THE JOURNAL OF PHYSICAL CHEMISTRY C
A JOURNAL OF THE AMERICAN CHEMICAL SOCIETY

pubs.acs.org/JPCC

Article

Molecular-Level Understanding of the Effect of Water on Oil Transport in Graphene Nanochannels

Zhihao Xu, Shiwen Wu, Siyu Tian, Dezhao Huang, Guoping Xiong,* and Tengfei Luo*

Cite This: *J. Phys. Chem. C* 2023, 127, 3671−3681

Read Online

ACCESS | Metrics & More | Article Recommendations

ABSTRACT: In this study, we used nonequilibrium molecular dynamics (NEMD) simulation to study the pressure-driven flow of oil in surface-functionalized graphene channels. We found that oil transport velocity could be improved by introducing water into the channel. Further study reveals two possible different mechanisms for the increased transport velocity of the water−oil system: On the one hand, the water film is formed between the oil and graphene substrates under driving force, which blocks the significant intermolecular interaction between the graphene layers and the oil molecules; on the other hand, the apparent viscosity of the liquid mixture is reduced by introducing water in the channel, which improves the efficiency of transport. Further comparative analysis on surfaces with different functional groups and oil with different polarities proves the universality of this water-induced flow transport enhancement of oil. The results may be useful for optimizing existing oil recovery devices to improve oil transport efficiencies.

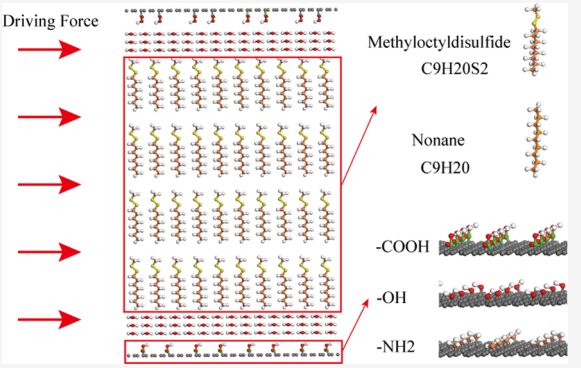

Downloaded via UNIV OF NOTRE DAME on June 24, 2023 at 22:28:44 (UTC).
See https://pubs.acs.org/sharingguidelines for options on how to legitimately share published articles.

1. INTRODUCTION

Petroleum will continue to be an inevitable part of the global energy landscape for the foreseeable future. Their exploitation and transportation have long been the focus of scientific research and engineering design. In order to address the challenges of the depleting conventional oil resources, unconventional oil such as shale oil[1,2] and offshore oil[3,4] has received increased attention.[5,6] Despite advances in equipment and technologies, the transport efficiency limits the recovery of the shale oil.[7−10] In addition, oil spills and leakage during offshore oil production or marine transportation can lead to tremendous losses of valuable resources and damage the environment.[11−13] Addressing these challenges calls for the understanding of fundamental oil transportation mechanisms in relevant conditions.

Over the past decade, nanofluid devices have attracted wide attention for their excellent performance and potential applications.[14−16] Holt et al.[17] and Xie et al.[18] reported extremely fast water transport in carbon nanotubes and graphene nanofluidic channels, suggesting their excellent potential for efficient fluid transport. To achieve enhanced oil recovery, nanoflooding using graphene has been studied.[19,20] For instance, Sikiru et al.[21] reported the great potential of graphene-driven oil recovery. Khoramian et al.[22] introduced graphene oxide nanosheets as a candidate for enhanced oil recovery. Wu et al.[23] also showed that the enhanced siphoning and capillarity of graphene nanostructures could be useful for energy-free oil spill recovery, and the oil spill recovery device designed by them could couple with renewable solar energy to enhance oil transport, which ensured the continuous, spontaneous oil transport in the recovery procedure.

Oil transport rate is influenced by the molecular level interactions between the oil molecules and the channel walls.[24] Stronger such interactions can lead to a stronger capillary effect, but on the other hand, it can also increase the resistance to the pressure-driven flow near the boundary, which can degrade the transport efficiency, especially inside nanochannels where the surface-to-volume ratios are large.[24,25] Tuning the surface chemistry of graphene nanosheets by chemical functionalization can change the wettability of the reservoir from oil-wet toward neural-wet or even water-wet[26,27] and effectively alter the interaction between oil and channels walls and thus influence the transport efficiency inside the channel.[28−31] In addition, the introduction of water has been widely adopted in oil recovery and has been proven to be an effective and economical technique for enhanced oil recovery.[32] Recent studies have shown that the role water plays in oil transport in shale inorganic nanopores was

Received: October 7, 2022
Revised: December 29, 2022
Published: February 10, 2023

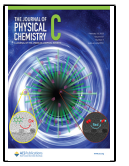

© 2023 American Chemical Society

https://doi.org/10.1021/acs.jpcc.2c07081
J. Phys. Chem. C 2023, 127, 3671−3681

underestimated and the introduction of water may also reduce the intermolecular interactions between oil molecules and the shale surfaces during transport.[25] However, the underlying mechanisms of the oil−water two-phase transport still need to be thoroughly understood.

In this work, molecular dynamics (MD) simulations are used to study the transport of oil molecules in the functionalized graphene nanochannels. Representative nonpolar and polar oil molecules are chosen for the simulations. Equilibrium molecular dynamics (EMD) simulations are performed to analyze the spatial distribution of water and oil molecules in the channel. The velocity distribution, density distribution, and viscosity of oil are calculated using nonequilibrium molecular dynamics (NEMD) simulations. We further investigate the effects of driving force, functional groups, and oil molecular polarity on the transport dynamics. The introduction of water molecules is found to significantly increase oil transport velocity under the same pressure. These results may provide new insights to the understanding of the mechanism of oil transport in graphene nanochannels.

2. MODELS AND METHODS

In this study, the model used for MD simulations consists of a nanochannel formed by two graphene sheets, in which oil and water molecules are placed. The system contains 160 oil molecules and 540 water molecules in total. Two kinds of oils, including methyloctyldisulfide[33] and nonane, are simulated to respectively represent polar and nonpolar oils (Figure 1).

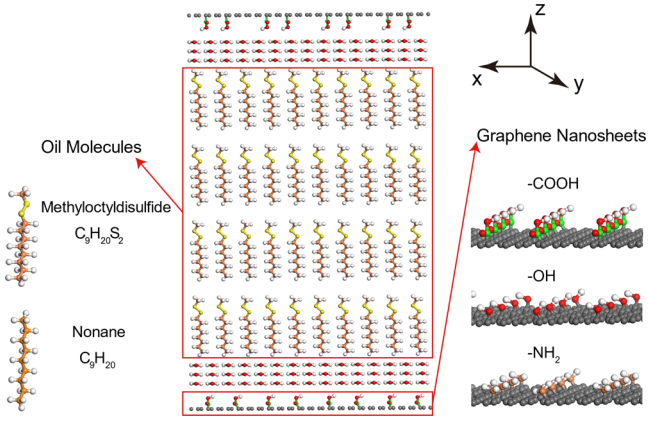

Figure 1. Simulation model (the channel functionalized by -COOH is shown as an example). Two different oils are simulated in this study: polarized methyloctyldisulfide ($C_9H_{20}S_2$) and nonpolarized nonane (C_9H_{20}). Three different functional groups on the graphene surfaces are studied: -COOH, -OH, and -NH_2.

When the polar oil is simulated, the mass fraction of oil is 76% in the oil−water mixture, and it is 68% when the nonpolar oil is simulated. The entire system is contained in a simulation box with dimensions of approximately 50 × 25 × 90 Å^3 (Figure 1), and periodic boundary conditions are employed in both the x and y directions of the simulation system. In the z direction, nonperiodic boundary conditions are used. To study the influence of interfacial interaction effect at the channel walls, three different functional groups with different hydrophilicities are adopted on the graphene sheets. These include the carboxyl group (-COOH), the hydroxyl group (-OH), and the amino group (-NH_2), and the surface densities of these functional groups are set at 0.0128/Å^2.

All simulations are conducted using the large-scale atom/molecule massively parallel simulator (LAMMPS).[34] The PCFF force field[35] is used to model the interactions between oil and the functional groups, while the Tersoff potential[36] is used to describe the interaction between carbon atoms in graphene layers. The SPC/E model is used for water,[37−41] and the SHAKE algorithm[42] is used to constrain the bond lengths and angles in water molecules. The nonbond interactions between different molecules are modeled using the Lennard-Jones potential with parameters derived from the Lorentz−Berthelot mixing rule:[43,44]

$$\sigma_{ij} = \frac{\sigma_{ii} + \sigma_{jj}}{2}, \ \varepsilon_{ij} = \sqrt{\varepsilon_{ii}\varepsilon_{jj}} \quad (1)$$

where σ_{ij} and ε_{ij} are the distance parameters and energy constants of the Lennard-Jones interactions between type i and type j atoms. The specific constants of each species are presented in Table 1.

Table 1. Pair Coefficients for the Oil−Water System

phase	site	ε (kJ/mol)	σ (Å)
graphene	C	0.054	4.010
oil	C	0.054	4.010
	S	0.071	4.027
	H	0.020	2.995
water	O	0.155	3.166
	H	0.000	0.000
-COOH	C	0.120	3.810
	O1	0.267	3.300
	O2	0.240	3.420
	H	0.013	1.110
-OH	O	0.240	3.420
	H	0.013	1.110
-NH2	N	0.065	4.070
	H	0.013	1.098

The simulation is divided into the equilibrium stage and simulation stage. Once the molecular structures are constructed, we use the conjugate gradient algorithm to minimize the potential energy of the initial configuration. In order to determine the distance between the two graphene sheets, we kept the lower graphene stationary and adjusted the position of the upper one. An NPT run at 300 K and 1 atm for 2 ns adjusts the distance between the two graphene sheets so the fluid in the nanochannel can achieve the target pressure at a given temperature.[45,46] When the distance between two nanosheets is stabilized, the systems are then further equilibrated in the NVT ensemble for 1 ns at the setting temperature, where a Nose−Hoover thermostat[47] holds the temperature at 300 K. Finally, we run the simulation for 100 ps under the NVE ensemble so that the atomic motion can recover the natural statistics without the influence of thermostats. For all simulations, a timestep size of 1 fs is used.

Since our purpose is to investigate the oil transport phenomenon in the channel and the effect of the introduction of water and the functional groups on the channel walls, the influence of temperature needs to be excluded, and the temperature of the liquid phase that is continuously driven by external force will blow up under the NVE ensemble. Therefore, after equilibration, EMD and NEMD simulations are performed under the NVT ensemble. The distance between the two graphene layers is fixed in these simulations.

https://doi.org/10.1021/acs.jpcc.2c07081
J. Phys. Chem. C 2023, 127, 3671−3681

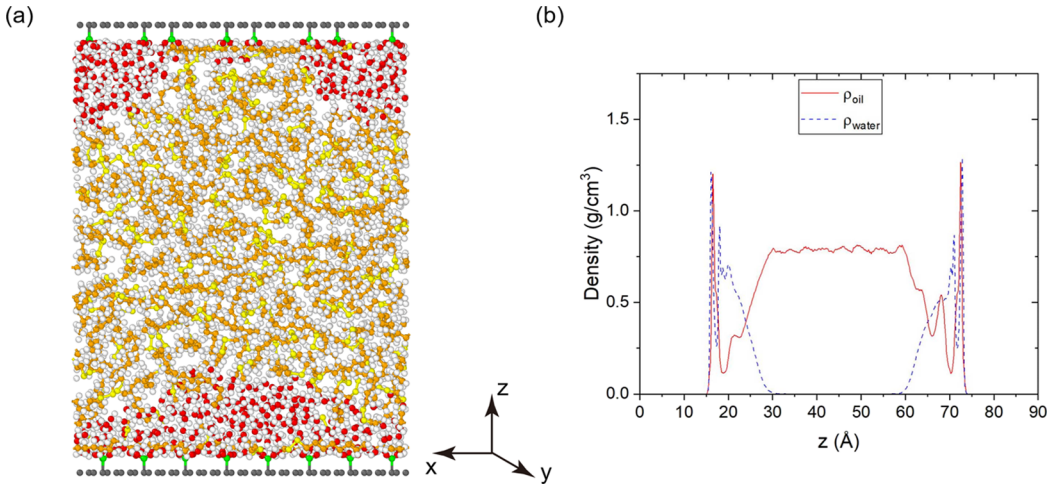

Figure 2. (a) Snapshot of the equilibrated system of the -COOH functionalized graphene nanochannel (the dark region represents the oil molecules, and light regions represent the water molecules); (b) static density distributions of water and oil in channels.

The EMD simulation is performed for 3 ns, and the trajectories are collected for analyzing the density profile in the channel. In the NEMD simulation, a constant external driving force along the x direction is applied to all the liquid molecules in the channel for 2 ns to simulate the flow driven by a uniform pressure. The magnitude of driving forces is determined by the relation:

$$\Delta P = F{\cdot}n/A \tag{2}$$

where A is the sectional area of the channel, ΔP is the pressure difference between two ends of the channel, and n represents the number of atoms in the liquid phase. Four different pressure differences are simulated in this work, which are 2 MPa (0.4 MPa/nm), 10 MPa (2 MPa/nm), 20 MPa (4 MPa/nm), and 40 MPa (8 MPa/nm). The corresponding driving forces applied on the liquid atoms are 1×10^{-4}, 5×10^{-4}, 1×10^{-3}, and $F = 2 \times 10^{-3}$ kcal/mol·Å. In the MD simulations, fluid temperature is usually calculated from atomic kinetic energy. However, the particle velocity along the direction of the driving force could be decomposed into the thermal velocity (the random movement related to temperature) and the flow velocity of center of mass (COM)[48] of the flowing particles. Therefore, we need to exclude the influence of COM movement when it comes to controlling and calculating fluid temperature in the NEMD simulations. Both using the velocity perpendicular to the flow direction[45,49,50] and subtracting the COM velocity[48] can help accurately control the temperature. Based on the works of Delhommelle et al.,[51,52] the first strategy would have better performance, which is adopted in the present study.

3. RESULTS AND DISCUSSION

3.1. Structural Properties. We take the model consisting of polar oil and -COOH functionalized graphene as the primary system and change the functional groups on the surface of the graphene and the types of oil in the channel to explore the influence of the hydrophilicity of the graphene sheets and the polarity of oil molecules. Figure 2a shows the configuration of the system after equilibration. Water is more likely to stay near the boundary of the liquid phase due to the hydrophilic functional group of -COOH. However, water molecules do not spread over the entire graphene surface but cluster like droplets close to the boundary of graphene (Figure 2a). Figure 2b shows the density profiles of water and oil molecules along the z direction inside the channel. The density of oil in the central region is constant but it starts to show layered structures near the graphene surface. The layered structures near the graphene surface are related to the fact that the oil molecules can be absorbed by the graphene layer, and the chain-like oil molecules can lay flat on the graphene surface. As some oil molecules lay flat on graphene, all atoms in these molecules are in close contact with graphene atoms and thus they have strong nonbond interactions between them. At the same time, it can be seen that high-density oil layers exist close to the graphene surface, which also suggests that the strong interaction between oil and graphene could be a significant resistance during pure oil transport.

We use equilibrium molecular dynamics (EMD) based on the Green−Kubo relation to calculate the viscosity of the oil in the bulk state and in the confined state, respectively. The confined state is represented by the same channel model with pure oil phase filled in it. Table 2 lists the results of viscosities. It can be seen that the viscosity of the oil confined in the channel differs slightly from the viscosity of oil in the bulk state. As the interaction between oil and wall increases, the viscosity of the confined state also increases slightly. Therefore, the viscosity of the oil in the nanochannel will change with the interaction between oil and the nanochannel wall. However, in these cases, the differences are very small.

Table 2. Viscosities of Oil in Bulk State and Confined States

state	bulk	confined (-COOH)	confined (-OH)	confined (-NH_2)
viscosity (mPa·s)	0.6810	0.7336	0.7021	0.6933

3.2. Velocity Analysis and Apparent Viscosity. Figure 3 shows the density profile of the polar oil and water molecules in the -COOH-functionalized graphene channel under different driving forces. The distribution is obtained by averaging the collected data over time during the last 2 ns of the NEMD simulation. Under a low driving force, the density profiles of oil and water are similar to those in the stationary state (Figure 2b) and not strictly symmetric. This is because we find the state of water and oil cannot remain stable near the two solid−liquid interfaces. Therefore, the two ends of the liquid region

https://doi.org/10.1021/acs.jpcc.2c07081
J. Phys. Chem. C 2023, 127, 3671−3681

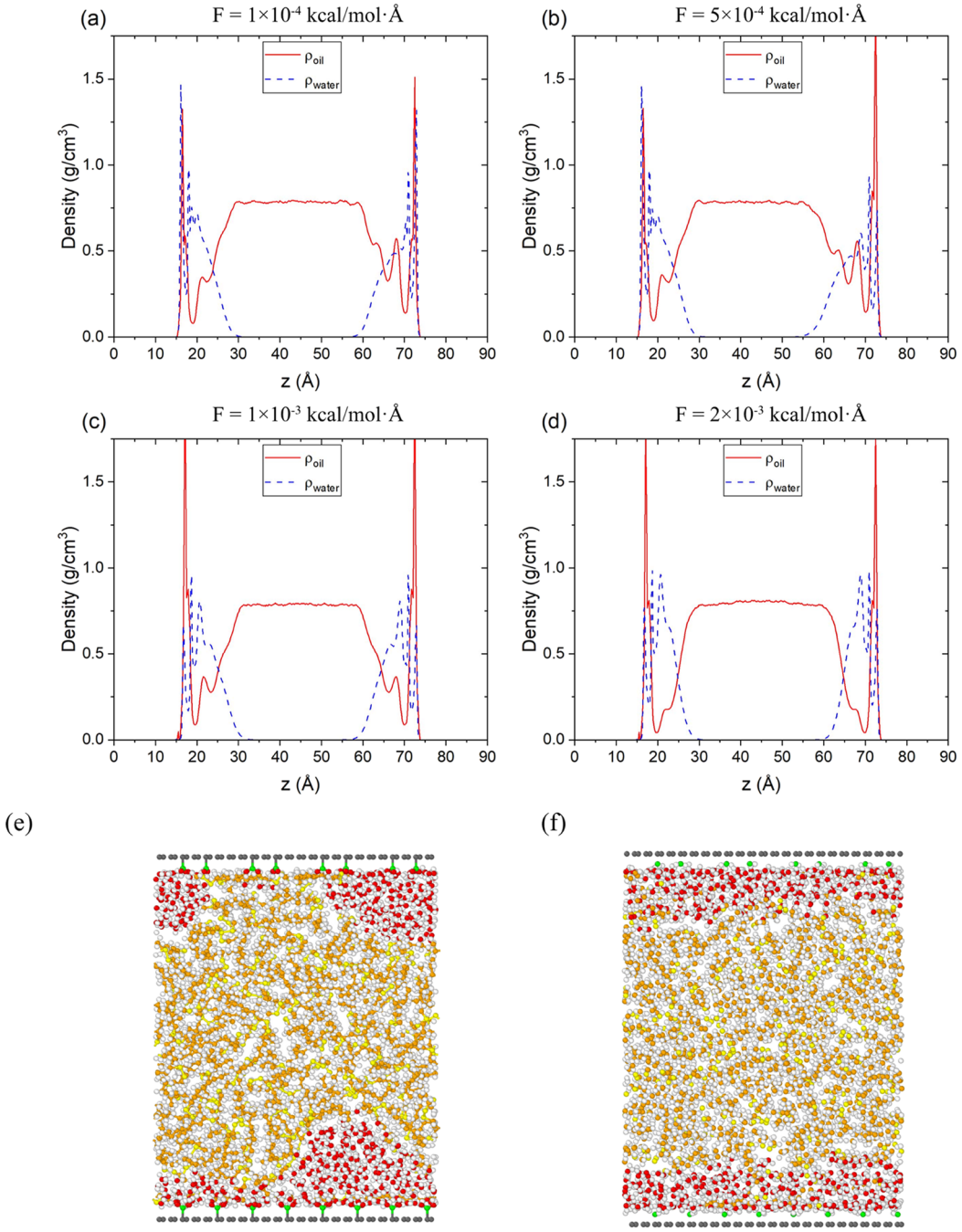

Figure 3. Density distributions of water and polarized oil molecules in a -COOH-functionalized graphene channel under different driving forces: (a) $F = 1 \times 10^{-4}$ kcal/mol·Å; (b) $F = 5 \times 10^{-4}$ kcal/mol·Å; (c) $F = 1 \times 10^{-3}$ kcal/mol·Å; (d) $F = 2 \times 10^{-3}$ kcal/mol·Å. (e, f) States of fluids before and after applying driving force of $F = 2 \times 10^{-3}$ kcal/mol·Å. There are two obvious and stable water films formed between oil and channel wall as seen in panel (f).

cannot maintain a consistent and stable distribution during the time of data collection. As the driving force increases (Figure 3a–d), both the density profiles of water and oil become more symmetric. The water density peaks at 5 Å away from the graphene surface start to emerge, which is related to the formation of two continuous water films in these locations (Figure 3e,f). With the formation of a continuous water films, the second peaks of the oil molecule distribution curves on both sides gradually flatten, suggesting that the intermolecular interactions between the oil molecules (except for the surface-attached oil molecules) and graphene nanosheets have been significantly reduced by the blocking effect of these water films, which leads to a lower drag force as oil molecules transport in graphene channels.

Under different driving forces, we plot the density distribution and velocity distribution profiles of oil along the z direction at the same time, as shown in Figure 4. The oil flow velocity increases with the increase of the driving force, which is not only related to the magnitude of driving force but also due to the formation of the stable water films that reduce the drag force at the oil–water boundaries and block the interaction between oil and the graphene channel walls. The velocity distribution tends to be more symmetric with the increase in the driving force as well, which is also due to the

https://doi.org/10.1021/acs.jpcc.2c07081
J. Phys. Chem. C 2023, 127, 3671–3681

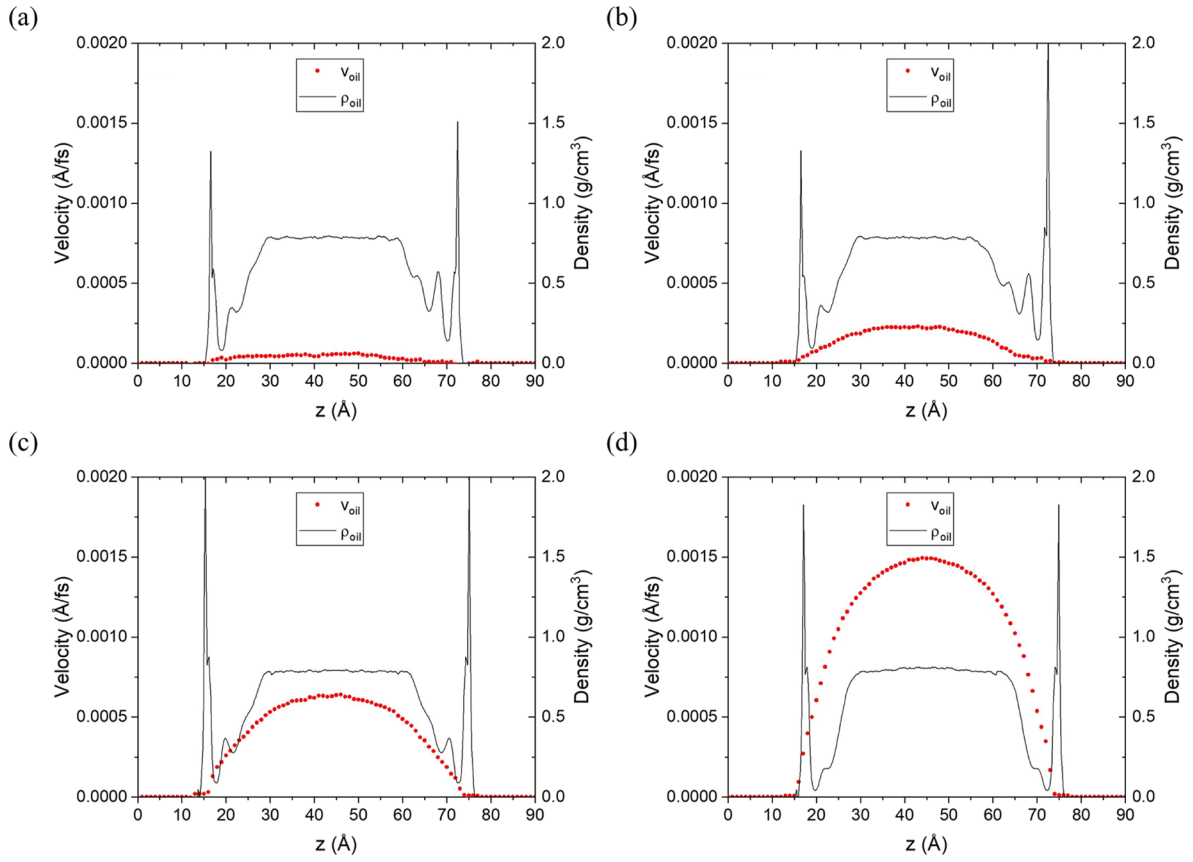

Figure 4. Velocity and density profiles of oil under different driving forces in the -COOH-functionalized channel: (a) $F = 1 \times 10^{-4}$ kcal/mol·Å; (b) $F = 5 \times 10^{-4}$ kcal/mol·Å; (c) $F = 1 \times 10^{-3}$ kcal/mol·Å; (d) $F = 2 \times 10^{-3}$ kcal/mol·Å. In the region of constant density, the velocity of oil could be fitted as a parabolic relation for calculating the apparent viscosity.

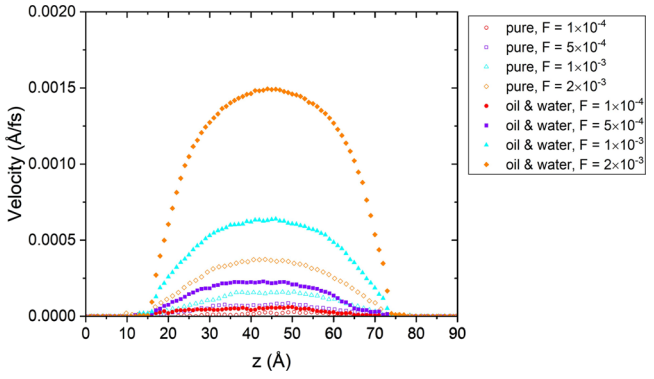

Figure 5. Comparison between the velocity of pure polarized oil and oil−water systems in -COOH-functionalized channel. The open symbols represent the velocity of pure oil, and the filled symbols represent the velocity of oil transport with water.

formation of stable water films that make the flow condition in the channel to be more steady.

As a comparison, we have studied pure oil flowing in the -COOH-functionalized nanochannel under the same driving forces. Figure 5 shows the oil velocity distribution for both the pure oil and oil−water mixture cases. Obviously, under the same driving forces, the oil flow velocities of the oil−water mixture cases are consistently higher than those in the pure oil cases, and larger driving force leads to greater differences in oil flow velocities. When the driving force is increased to 2×10^{-3} kcal/mol·Å, water molecules can spread over the whole

Table 3. Calculated Apparent and Center Portion Viscosities of Oil in Pure Oil and an Oil−Water Mixture Flowing in the Graphene Nanochannel[a]

	pure oil		oil & water	
driving force (kcal/mol·Å)	apparent viscosity (mPa·s)	central viscosity (mPa·s)	apparent viscosity (mPa·s)	central viscosity (mPa·s)
bulk		0.6810		0.6810
1×10^{-4}	0.6433	0.6441	0.6382	0.6433
5×10^{-4}	0.6360	0.6401	0.6097	0.6357
1×10^{-3}	0.6131	0.6337	0.5181	0.6285
2×10^{-3}	0.5816	0.6300	0.4640	0.6201

[a]The viscosity of bulk oil is from Riddick et al.

graphene surfaces and form stable water films (Figure 3f). In this case, the oil flow velocity in the channel center can differ by nearly six-fold in these two cases. For the oil−water mixture cases, in the central region of the channel, the oil density remains constant and close to the bulk density of $C_9H_{20}S_2$ in the natural state (Figure 4), that is, the oil in this region can still maintain its intrinsic properties in the transport. The viscosity can be calculated by fitting the velocity with a parabolic function as shown by eq 3.[53]

$$v = az^2 + c \tag{3}$$

where a and c are fitting parameters. The apparent viscosity of the oil in the channel can then be obtained by

https://doi.org/10.1021/acs.jpcc.2c07081
J. Phys. Chem. C 2023, 127, 3671−3681

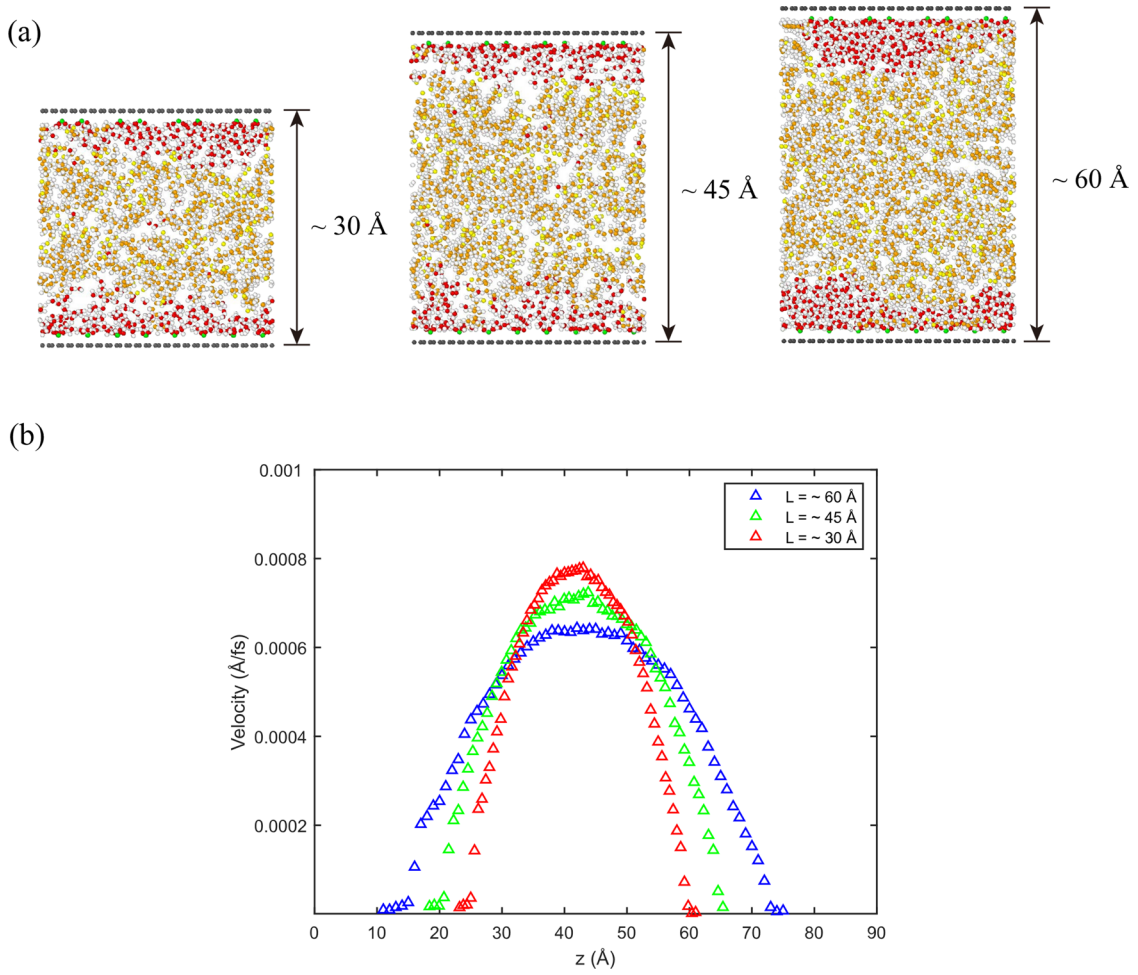

Figure 6. (a) Comparison between three different channels with different widths. (b) Velocity profile of oil in three channels.

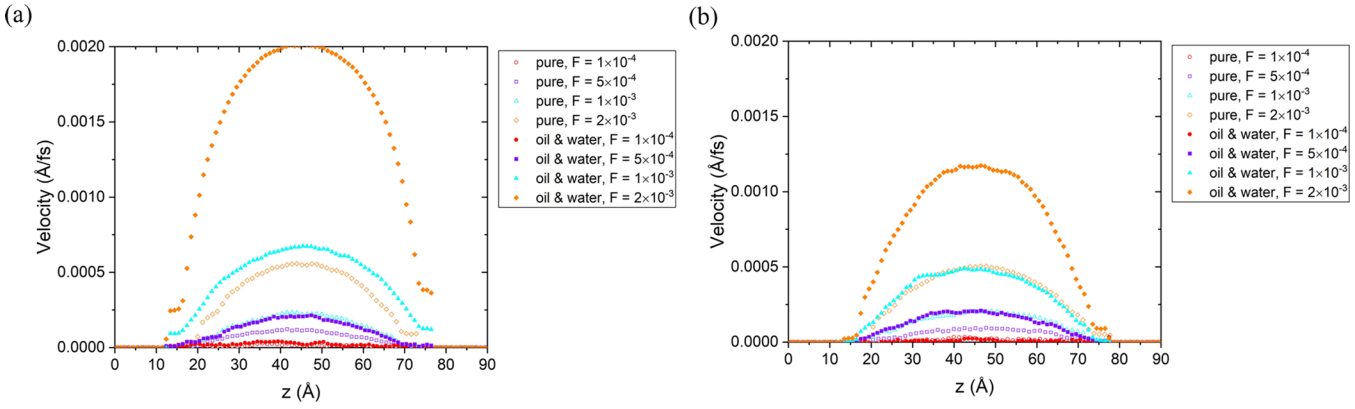

Figure 7. Comparison between the velocity of pure polarized oil and oil−water systems in the (a) -OH channel and (b) -NH_2 channel.

$$\eta = -\frac{F\rho}{2a} \tag{4}$$

where F is the driving force along the x direction and ρ is the density of oil.

We extract the overall apparent viscosity and the center portion viscosity by fitting all the velocity data points over the whole width of the channel and only the center portion where density profiles are constant (two cases are shown later in Figure 8), respectively. The results are shown in Table 3 together with the comparison to the viscosity of bulk oil from Table 2. Our calculated viscosities are close to the calculated value of bulk oil. Both the apparent viscosity and the center portion viscosity decrease as the driving force increases, which can be attributed to the shear thinning phenomenon. The apparent viscosities are always lower than their center portion counterparts. This is because oil molecules close to the graphene walls tend to have reduced velocities (e.g., see Figure 5). For the center portion viscosities, both the values and the decreasing trends are similar for the pure oil and oil−water mixture cases. Interestingly, comparing the apparent viscosities in these two cases, it is obvious that the decrease in viscosity as

https://doi.org/10.1021/acs.jpcc.2c07081
J. Phys. Chem. C 2023, 127, 3671−3681

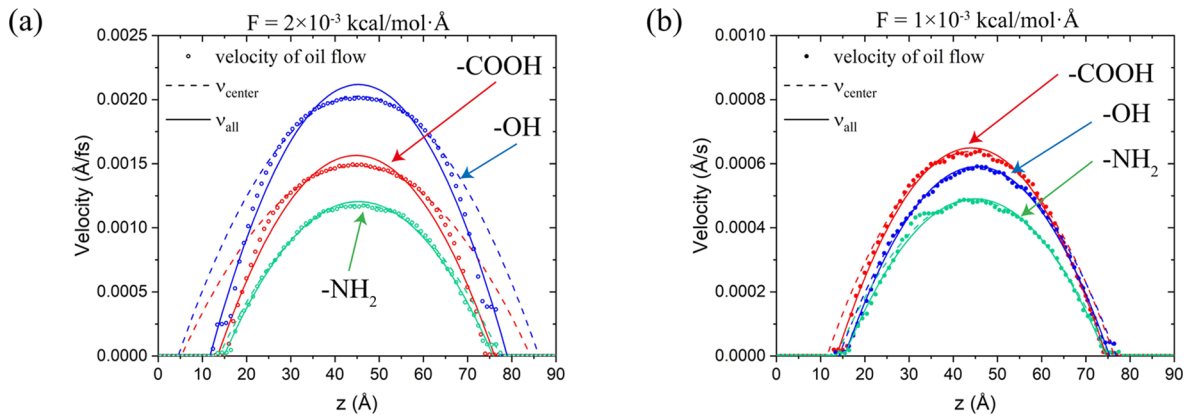

Figure 8. Fitting for oil velocity under different driving forces: (a) $F = 2 \times 10^{-3}$ kcal/mol·Å and (b) $F = 1 \times 10^{-3}$ kcal/mol·Å. Obvious divergence between central viscosity and apparent viscosity fitted by center velocity and all the velocity can be observed. In addition, under large driving force, the -OH-functionalized channel shows an exceptional performance of oil transport, while under relatively lower driving forces, oil transport velocity is still consistent with the hydrophilicity of channel walls.

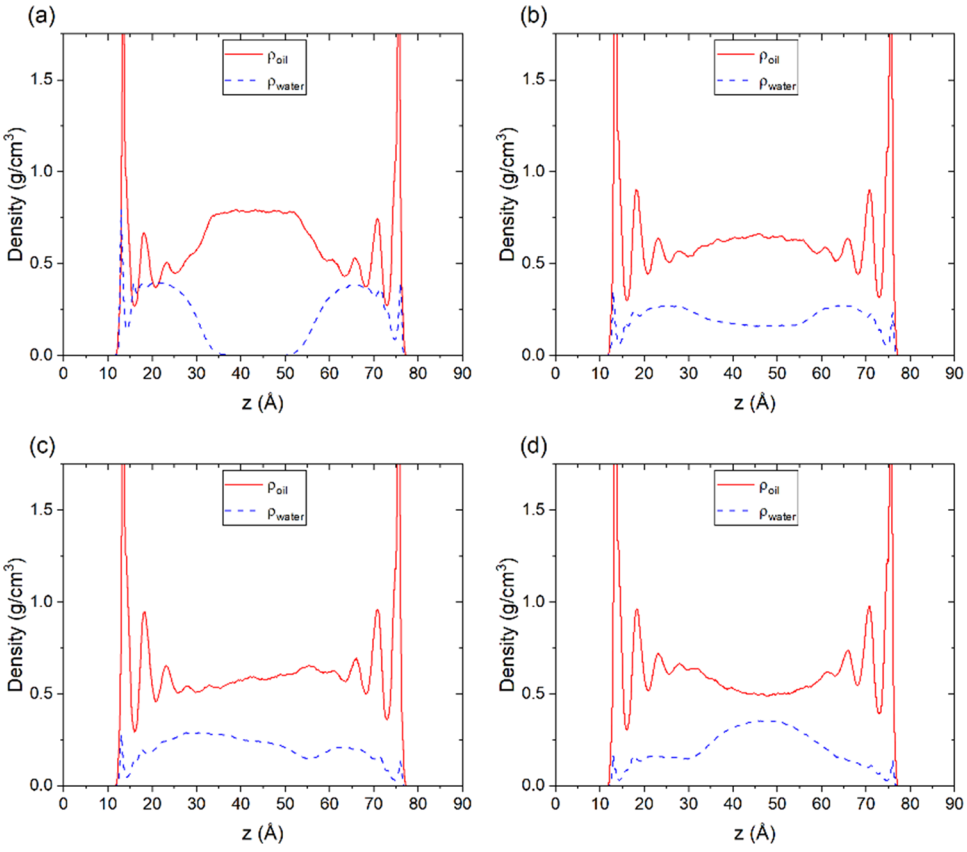

Figure 9. Density distribution in the -NH_2 channel under different driving forces: (a) $F = 1 \times 10{-}4$ kcal/mol·Å; (b) $F = 5 \times 10{-}4$ kcal/mol·Å; (c) $F = 1 \times 10{-}3$ kcal/mol·Å; (d) $F = 2 \times 10{-}3$ kcal/mol·Å.

driving force increases is much more dramatic in the oil−water mixture case than in the pure oil case. This should be related to the observed water film formation phenomena in the high driving forces in the oil−water mixture. These formed water layers greatly reduce the interatomic interactions between oil molecules and the graphene walls. The oil molecules in these cases mainly interact with the water layer, which is fluidic and flows. Therefore, the oil can flow with less boundary resistance and thus shows lower apparent viscosity. Such an observation is not obvious for the center portion viscosities since their calculations have excluded the boundary effects.

The width of the channels also potentially has an effect on the transport of oil. Under the same driving pressure (20 MPa), three channels with different widths (as shown in Figure 6a) are filled with the same ratio of oil and water molecules. The velocity profiles of the oil are shown in Figure 6b. It can be seen that as the channel width decreases, the oil transport velocity increases. This may be attribute to the weaker wall effect in wider channels.

To verify that the transport enhancement effect caused by the water film is universal for channel surfaces with different hydrophilicities, we performed the same simulation in the

https://doi.org/10.1021/acs.jpcc.2c07081
J. Phys. Chem. C 2023, 127, 3671−3681

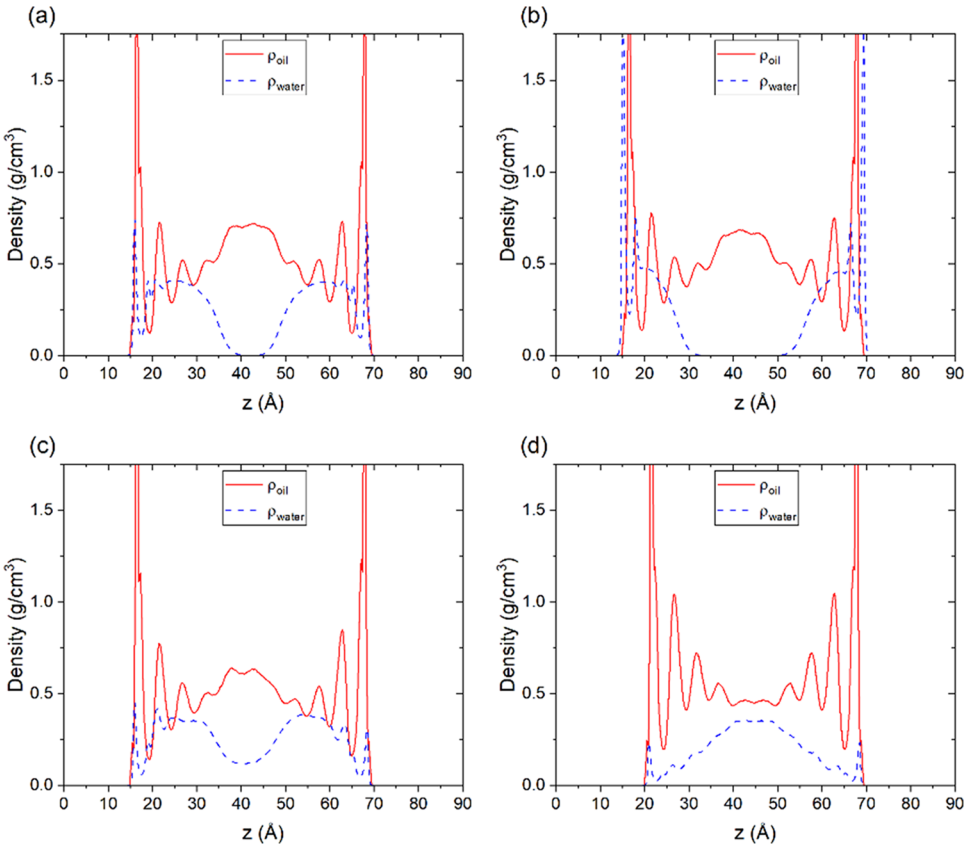

Figure 10. Density distributions of water and nonpolarized oil molecules in the -COOH-functionalized channel under different driving forces: (a) $F = 1 \times 10^{-4}$ kcal/mol·Å; (b) $F = 5 \times 10^{-4}$ kcal/mol·Å; (c) $F = 1 \times 10^{-3}$ kcal/mol·Å; (d) $F = 2 \times 10^{-3}$ kcal/mol·Å.

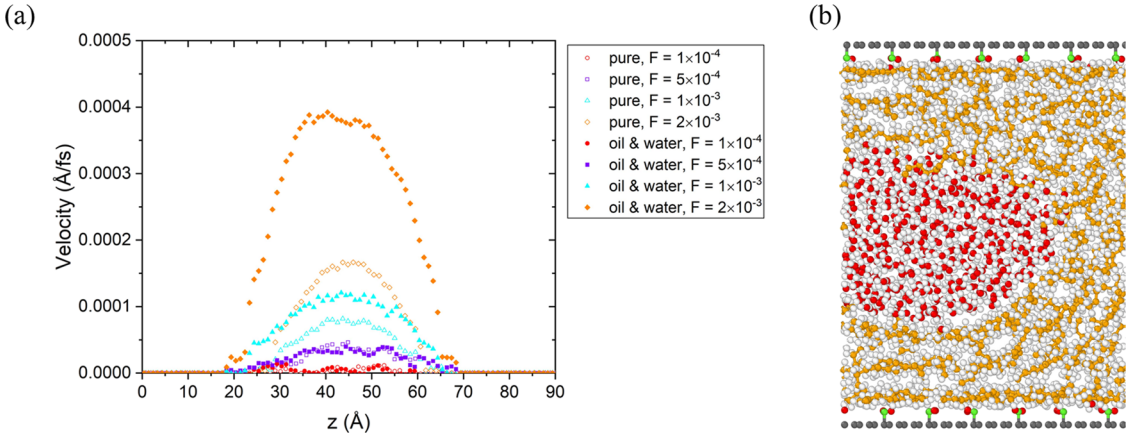

Figure 11. (a) Velocity profiles of pure oil and water−oil systems in the -COOH-functionalized graphene channel. The oil here is nonpolarized nonane. (b) Snapshot of flow conditions under $F = 2 \times 10^{-3}$ kcal/mol·Å. Water molecules have entered the central region of the channel and formed a water cluster flowing with oil.

-OH-functionalized and the -NH_2-functionalized graphene nanochannels. Figure 7 compares the velocity of oil in pure oil and oil−water mixture cases for both channels. In both channels, larger driving force leads to higher flow velocities, and more importantly, the introduction of water can significantly increase the oil flow velocity. It is noteworthy that with the decrease of the functional group hydrophilicity (-COOH > -OH > -NH_2), the oil flow velocity decreases as well under low driving force ($F \leq 1 \times 10^{-3}$ kcal/mol·Å), as shown in Figure 8b, but when the driving force is increased to 2×10^{-3} kcal/mol·Å, the transport velocity in the -OH-functionalized channel becomes extremely large (shown in Figure 8a). This may be because in this case, the water film can still form stably, but the intermolecular interaction between oil and the functional groups is greatly reduced, which could be seen from the fact that the velocity of pure oil in the -OH channel is larger than that in the -COOH channel under larger driving force. Therefore, even though the shielding effect of the water film in this case is not as good as that in the -COOH channel, the overall transport velocity can be greatly increased.

Another interesting phenomenon is that in the -NH_2 channel, although the flow velocity has increased, it is not

https://doi.org/10.1021/acs.jpcc.2c07081
J. Phys. Chem. C 2023, 127, 3671−3681

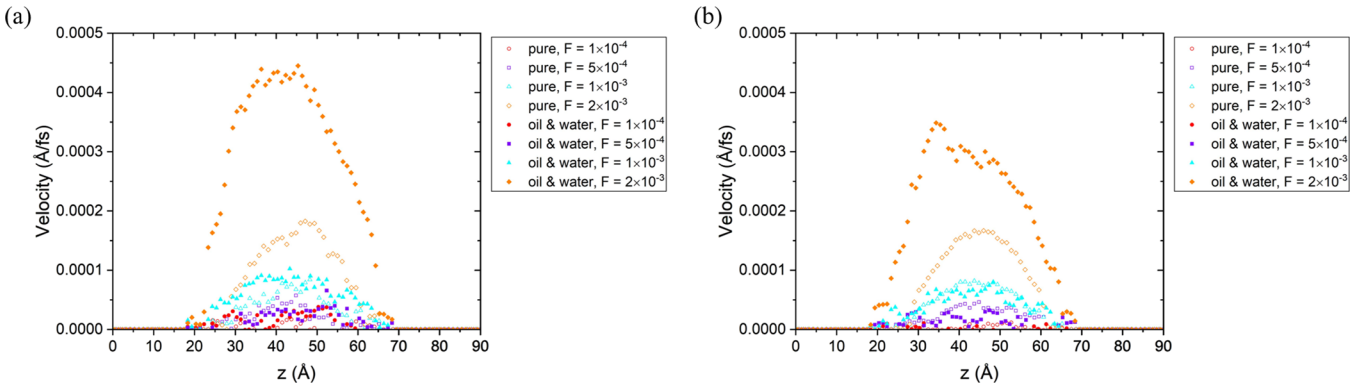

Figure 12. Velocity profiles of pure oil and oil−water in the (a) -OH channel and (b) -NH_2-functionalized channel. The oil here is nonpolarized nonane.

attributed to the water film shielding effect. Figure 9 shows the density profile of oil and water in the -NH_2 channel. With the increase in the driving force, water molecules do not spread to form continuous films. Instead, they aggregate into a water cluster, which floats inside the oil phase. This is related to the weaker interaction between the -NH_2 group and water molecules compared to the other two more hydrophilic functional groups (i.e., -CH_2 and -COOH).

We further simulated the transport of nonpolar nonane (C_9H_{20}) molecules in the graphene nanochannel. We first simulate the -COOH-functionalized channel and apply different driving forces to study the velocity and density profiles. Figure 10 shows the density profiles of oil and water in the channel. It can be seen from the absorption peaks, which have significant oscillations, that for nonpolar alkane, there is a more intimate contact between graphene layers and the oil molecules. Therefore, in the competition between oil and water at the graphene surface, oil molecules can cover more space and thus water molecules are more difficult to be held by the -COOH groups on the graphene surface. This weakened interaction allows water molecules to move to the center of the channel instead of forming clusters or continuous films in the vicinity of the graphene surface, which can be seen in Figure 10c,d.

However, the introduction of water can still increase the flow velocity of oil. Figure 11a shows the oil flow velocity profiles in the pure oil and oil−water mixture systems under different driving forces. Under low driving forces ($F = 1 \times 10^{-4}$ and 5×10^{-4} kcal/mol·Å), the introduction of water does not significantly affect the flow velocity because it does not weaken the strong intermolecular interaction between oil and graphene. As the driving force increases, water molecules migrate to the center of the channel and form a cluster (Figure 11b), increasing the oil flow velocity.

We also simulated the flow of nonane in the other two graphene nanochannels modified by -OH and -NH_2. Figure 12 shows the flow velocity profiles. In both cases, the oil flow velocity also greatly increases after the introduction of water, especially with the large driving forces. The velocity profile of the nonpolar alkane is not as symmetric as the polar oil, which indicates that the oil flow in the channel is not stable. This finding agrees well with the fact that stable water films cannot be formed. Therefore, for nonpolar alkanes, the enhancement in the transport velocity is caused by water clusters in the center of the channel rather than the water films at the boundary. It is known that mixing water with oil can lead to reduced viscosity.[54]

4. CONCLUSIONS

In summary, when oil transports in graphene channels, if hydrophilic functional groups are added to the graphene surface and water is introduced into the channel, the oil transport velocity will be greatly increased under the same driving force. If the hydrophilicity of functional groups on the surface is high or the adsorption of oil molecules on the graphene surface is not significant, water molecules will form water films at boundaries, thus shielding the interaction between the graphene layers and oil molecules. Therefore, the transport velocity of oil in the channel is greatly increased. However, when the hydrophilicity of functional groups is lower or the adsorption of oil molecules on graphene layers is significant, water will not be stable at the boundary and will move into the central region of the channel to form clusters. In this case, the oil transport velocity will also increase due to reduced effective viscosity of the oil−water mixture. Therefore, the introduction of hydrophilic functional groups and water can greatly improve the recovery efficiency of oil. Our research results can provide new insights for the optimization of existing oil spill recovery devices and greatly improve the efficiency of oil spill recovery.

AUTHOR INFORMATION

Corresponding Authors

Guoping Xiong − *Department of Mechanical Engineering, The University of Texas at Dallas, Richardson, Texas 75080, United States*; Email: guoping.xiong@utdallas.edu

Tengfei Luo − *Department of Aerospace and Mechanical Engineering, University of Notre Dame, Notre Dame, Indiana 46556, United States*; orcid.org/0000-0003-3940-8786; Email: tluo@nd.edu

Authors

Zhihao Xu − *Department of Aerospace and Mechanical Engineering, University of Notre Dame, Notre Dame, Indiana 46556, United States*; orcid.org/0000-0003-1054-3669

Shiwen Wu − *Department of Mechanical Engineering, The University of Texas at Dallas, Richardson, Texas 75080, United States*; orcid.org/0000-0001-8065-0684

Siyu Tian − *Department of Mechanical Engineering, The University of Texas at Dallas, Richardson, Texas 75080, United States*; orcid.org/0000-0001-6463-0691

https://doi.org/10.1021/acs.jpcc.2c07081
J. Phys. Chem. C 2023, 127, 3671−3681

Dezhao Huang − *Department of Aerospace and Mechanical Engineering, University of Notre Dame, Notre Dame, Indiana 46556, United States;* orcid.org/0000-0002-1413-5438

Complete contact information is available at: https://pubs.acs.org/10.1021/acs.jpcc.2c07081

Notes

The authors declare no competing financial interest.

■ ACKNOWLEDGMENTS

The authors thank the National Science Foundation (grant nos. CBET-1949962 and 1949910) for support. The simulations were supported by the Notre Dame Center for Research Computing and NSF through XSEDE computing resources provided by TACC Stampede II under Grant No. TG-CTS100078.

■ REFERENCES

(1) Hughes, J. D. A reality check on the shale revolution. *Nature* **2013**, *494*, 307−308.
(2) Burnham, A.; Han, J.; Clark, C. E.; Wang, M.; Dunn, J. B.; Palou-Rivera, I. Life-Cycle Greenhouse Gas Emissions of Shale Gas, Natural Gas, Coal, and Petroleum. *Environ. Sci. Technol.* **2012**, *46*, 619−627.
(3) Cornford, C.; Birdsong, B.; Groves-Gidney, M., Offshore Unconventional Oil From the Kimmeridge Clay Formation of the North Sea: A Technical and Economic Case. In *SPE/AAPG/SEG Unconventional Resources Technology Conference*, 2014; OnePetro, pp URTEC-1936282-MS.
(4) Wang, P.; Chen, Z.; Jin, Z.; Jiang, C.; Sun, M.; Guo, Y.; Chen, X.; Jia, Z. Shale oil and gas resources in organic pores of the Devonian Duvernay Shale, Western Canada Sedimentary Basin based on petroleum system modeling. *J. Nat. Gas Sci. Eng.* **2018**, *50*, 33−42.
(5) Mohaghegh, S. D. Reservoir modeling of shale formations. *J. Nat. Gas Sci. Eng.* **2013**, *12*, 22−33.
(6) Jiang, X. M.; Han, X. X.; Cui, Z. G. New technology for the comprehensive utilization of Chinese oil shale resources. *Energy* **2007**, *32*, 772−777.
(7) Javadpour, F.; Fisher, D.; Unsworth, M., Nanoscale Gas Flow in Shale Gas Sediments. *J. Can. Pet. Technol.* **2007**, *46* (), DOI: 10.2118/07-10-06.
(8) Wang, S.; Feng, Q.; Javadpour, F.; Zha, M.; Cui, R. Multiscale Modeling of Gas Transport in Shale Matrix: An Integrated Study of Molecular Dynamics and Rigid-Pore-Network Model. *SPE J.* **2020**, *25*, 1416−1442.
(9) Falk, K.; Coasne, B.; Pellenq, R.; Ulm, F.-J.; Bocquet, L. Subcontinuum mass transport of condensed hydrocarbons in nanoporous media. *Nat. Commun.* **2015**, *6*, 694910.
(10) Hantal, G.; Brochard, L.; Dias Soeiro Cordeiro, M. N.; Ulm, F. J.; Pellenq, R. J. M. Surface Chemistry and Atomic-Scale Reconstruction of Kerogen−Silica Composites. *J. Phys. Chem. C* **2014**, *118*, 2429−2438.
(11) Whitfield, J. How to clean a beach. *Nature* **2003**, *422*, 464−466.
(12) Jernelöv, A. How to defend against future oil spills. *Nature* **2010**, *466*, 182−183.
(13) Ma, Q.; Cheng, H.; Fane, A. G.; Wang, R.; Zhang, H. Recent Development of Advanced Materials with Special Wettability for Selective Oil/Water Separation. *Small* **2016**, 2186.
(14) Werber, J. R.; Osuji, C. O.; Elimelech, M. Materials for next-generation desalination and water purification membranes. *Nat. Rev. Mater.* **2016**, *1*, 16018.
(15) Faucher, S.; Aluru, N.; Bazant, M. Z.; Blankschtein, D.; Brozena, A. H.; Cumings, J.; Pedro de Souza, J.; Elimelech, M.; Epsztein, R.; Fourkas, J. T.; Rajan, A. G.; Kulik, H. J.; Levy, A.; Majumdar, A.; Martin, C.; McEldrew, M.; Misra, R. P.; Noy, A.; Pham, T. A.; Reed, M.; Schwegler, E.; Siwy, Z.; Wang, Y.; Strano, M. Critical Knowledge Gaps in Mass Transport through Single-Digit Nanopores: A Review and Perspective. *J. Phys. Chem. C* **2019**, *123*, 21309−21326.
(16) Bansal, R. C.; Goyal, M., *Activated carbon adsorption*. CRC press: 2005, DOI: 10.1201/9781420028812.
(17) Holt, J. K.; Park, H. G.; Wang, Y.; Stadermann, M.; Artyukhin, A. B.; Grigoropoulos, C. P.; Noy, A.; Bakajin, O. Fast Mass Transport Through Sub-2-Nanometer Carbon Nanotubes. *Science* **2006**, *312*, 1034−1037.
(18) Xie, Q.; Alibakhshi, M. A.; Jiao, S.; Xu, Z.; Hempel, M.; Kong, J.; Park, H. G.; Duan, C. Fast water transport in graphene nanofluidic channels. *Nat. Nanotechnol.* **2018**, *13*, 238−245.
(19) Le, N. Y. T.; Pham, D. K.; Le, K. H.; Nguyen, P. T. Design and screening of synergistic blends of SiO 2 nanoparticles and surfactants for enhanced oil recovery in high-temperature reservoirs. *Adv. Nat. Sci.: Nanosci. Nanotechnol.* **2011**, *2*, No. 035013.
(20) Zhang, T.; Davidson, A.; Bryant, S. L.; Huh, C., Nanoparticle-Stabilized Emulsions for Applications in Enhanced Oil Recovery. In *SPE Improved Oil Recovery Symposium*, 2010; OnePetro, pp SPE-129885-MS.
(21) Sikiru, S.; Rostami, A.; Soleimani, H.; Yahya, N.; Afeez, Y.; Aliu, O.; Yusuf, J. Y.; Oladosu, T. L. Graphene: Outlook in the enhance oil recovery (EOR). *J. Mol. Liq.* **2021**, *321*, No. 114519.
(22) Khoramian, R.; Ramazani S A, A.; Hekmatzadeh, M.; Kharrat, R.; Asadian, E. Graphene Oxide Nanosheets for Oil Recovery. *ACS Appl. Nano Mater.* **2019**, *2*, 5730−5742.
(23) Wu, S.; Yang, H.; Xiong, G.; Tian, Y.; Gong, B.; Luo, T.; Fisher, T. S.; Yan, J.; Cen, K.; Bo, Z.; Ostrikov, K. K. Spill-SOS: Self-Pumping Siphon-Capillary Oil Recovery. *ACS Nano* **2019**, *13*, 13027−13036.
(24) Zheng, H.; Du, Y.; Xue, Q.; Zhu, L.; Li, X.; Lu, S.; Jin, Y. Surface Effect on Oil Transportation in Nanochannel: a Molecular Dynamics Study. *Nanoscale Res. Lett.* **2017**, *12*, 413.
(25) Zhang, W.; Feng, Q.; Jin, Z.; Xing, X.; Wang, S. Molecular simulation study of oil-water two-phase fluid transport in shale inorganic nanopores. *Chem. Eng. Sci.* **2021**, *245*, No. 116948.
(26) Samanta, A.; Ojha, K.; Sarkar, A.; Mandal, A. Surfactant and surfactant-polymer flooding for enhanced oil recovery. *Adv. Pet. Explor. Dev.* **2011**, *2*, 13−18.
(27) Donaldson, E. C.; Chilingarian, G. V.; Yen, T. F., *Enhanced oil recovery, II: Processes and operations*. Elsevier: 1989.
(28) Wu, S.; Xiong, G.; Yang, H.; Gong, B.; Tian, Y.; Xu, C.; Wang, Y.; Fisher, T.; Yan, J.; Cen, K.; Luo, T.; Tu, X.; Bo, Z.; Ostrikov, K. Multifunctional Solar Waterways: Plasma-Enabled Self-Cleaning Nanoarchitectures for Energy-Efficient Desalination. *Adv. Energy Mater.* **2019**, *9*, No. 1901286.
(29) Wu, S.; Xiong, G.; Yang, H.; Tian, Y.; Gong, B.; Wan, H.; Wang, Y.; Fisher, T. S.; Yan, J.; Cen, K.; Bo, Z.; Ostrikov, K. Scalable Production of Integrated Graphene Nanoarchitectures for Ultrafast Solar-Thermal Conversion and Vapor Generation. *Matter* **2019**, *1*, 1017−1032.
(30) Xiong, G.; He, P.; Lyu, Z.; Chen, T.; Huang, B.; Chen, L.; Fisher, T. S. Bioinspired leaves-on-branchlet hybrid carbon nanostructure for supercapacitors. *Nat. Commun.* **2018**, *9*, 790.
(31) Xiong, G.; Meng, C.; Reifenberger, R. G.; Irazoqui, P. P.; Fisher, T. S. Graphitic Petal Electrodes for All-Solid-State Flexible Supercapacitors. *Adv. Energy Mater.* **2014**, *4*, No. 1300515.
(32) Pope, G. A. The Application of Fractional Flow Theory to Enhanced Oil Recovery. *Soc. Pet. Eng. J.* **1980**, *20*, 191−205.
(33) Sedghi, M.; Piri, M.; Goual, L. Atomistic Molecular Dynamics Simulations of Crude Oil/Brine Displacement in Calcite Mesopores. *Langmuir* **2016**, *32*, 3375−3384.
(34) Plimpton, S. Fast Parallel Algorithms for Short-Range Molecular Dynamics. *J. Comput. Phys.* **1995**, *117*, 1−19.
(35) Sun, H.; Mumby, S. J.; Maple, J. R.; Hagler, A. T. An ab Initio CFF93 All-Atom Force Field for Polycarbonates. *J. Am. Chem. Soc.* **1994**, *116*, 2978−2987.
(36) Tersoff, J. Modeling solid-state chemistry: Interatomic potentials for multicomponent systems. *Phys. Rev. B* **1989**, *39*, 5566−5568.

(37) Berendsen, H. J.; Postma, J. P.; van Gunsteren, W. F.; Hermans, J., Interaction models for water in relation to protein hydration. In *Intermolecular forces : proceedings of the fourteenth Jerusalem symposium on quantum chemistry and biochemistry held in jerusalem*, Springer: 1981; pp. 331−342, DOI: 10.1007/978-94-015-7658-1_21.
(38) Taylor, R. S.; Dang, L. X.; Garrett, B. C. Molecular Dynamics Simulations of the Liquid/Vapor Interface of SPC/E Water. *J. Phys. Chem.* **1996**, *100*, 11720−11725.
(39) Jaffe, R. L.; Gonnet, P.; Werder, T.; Walther, J. H.; Koumoutsakos, P. Water−Carbon Interactions 2: Calibration of Potentials using Contact Angle Data for Different Interaction Models. *Mol. Simul.* **2004**, *30*, 205−216.
(40) Werder, T.; Walther, J. H.; Jaffe, R. L.; Halicioglu, T.; Koumoutsakos, P. On the Water−Carbon Interaction for Use in Molecular Dynamics Simulations of Graphite and Carbon Nanotubes. *J. Phys. Chem. B* **2003**, *107*, 1345−1352.
(41) Werder, T.; Walther, J. H.; Jaffe, R. L.; Halicioglu, T.; Noca, F.; Koumoutsakos, P. Molecular Dynamics Simulation of Contact Angles of Water Droplets in Carbon Nanotubes. *Nano Lett.* **2001**, *1*, 697−702.
(42) Ryckaert, J.-P.; Ciccotti, G.; Berendsen, H. J. C. Numerical integration of the cartesian equations of motion of a system with constraints: molecular dynamics of n-alkanes. *J. Comput. Phys.* **1977**, *23*, 327−341.
(43) Lorentz, H. A. Ueber die Anwendung des Satzes vom Virial in der kinetischen Theorie der Gase. *Ann. Phys.* **1881**, *248*, 127−136.
(44) Berthelot, D. Sur la Détermination Rigoureuse des Poids Moléculaires sentent par Rapport à la Loi de Mariotte. *Compt. Rendus* **1898**, *126*, 954−956.
(45) Falk, K.; Sedlmeier, F.; Joly, L.; Netz, R. R.; Bocquet, L. Ultralow Liquid/Solid Friction in Carbon Nanotubes: Comprehensive Theory for Alcohols, Alkanes, OMCTS, and Water. *Langmuir* **2012**, *28*, 14261−14272.
(46) Wei, N.; Peng, X.; Xu, Z. Breakdown of fast water transport in graphene oxides. *Phys. Rev. E* **2014**, *89*, No. 012113.
(47) Hoover, W. G. Canonical dynamics: Equilibrium phase-space distributions. *Phys. Rev. A* **1985**, *31*, 1695−1697.
(48) Wang, S.; Javadpour, F.; Feng, Q. Molecular dynamics simulations of oil transport through inorganic nanopores in shale. *Fuel* **2016**, *171*, 74−86.
(49) Boţan, A.; Rotenberg, B.; Marry, V.; Turq, P.; Noetinger, B. Hydrodynamics in Clay Nanopores. *J. Phys. Chem. C* **2011**, *115*, 16109−16115.
(50) Předota, M.; Cummings, P. T.; Wesolowski, D. J. Electric Double Layer at the Rutile (110) Surface. 3. Inhomogeneous Viscosity and Diffusivity Measurement by Computer Simulations. *J. Phys. Chem. C* **2007**, *111*, 3071−3079.
(51) Delhommelle, J. Simulations of shear-induced melting in two dimensions. *Phys. Rev. B* **2004**, *69*, No. 144117.
(52) Delhommelle, J. Should "lane formation" occur systematically in driven liquids and colloids? *Phys. Rev. E* **2005**, *71*, No. 016705.
(53) Wang, S.; Liang, Y.; Feng, Q.; Javadpour, F. Sticky layers affect oil transport through the nanopores of realistic shale kerogen. *Fuel* **2022**, *310*, No. 122480.
(54) Wen, J.; Zhang, J.; Wei, M. Effective viscosity prediction of crude oil-water mixtures with high water fraction. *J. Pet. Sci. Eng.* **2016**, *147*, 760−770.

Recommended by ACS

Nanoscale Contact Line Pinning Boosted by Ångström-Scale Surface Heterogeneity
Yuta Heima, Koji Takahashi, *et al.*
APRIL 05, 2023
THE JOURNAL OF PHYSICAL CHEMISTRY LETTERS
READ

Impact Dynamics of Non-Newtonian Droplets on Superhydrophobic Surfaces
Mehdi H. Biroun, Yong-Qing Fu, *et al.*
APRIL 11, 2023
LANGMUIR
READ

Scale Effect of Surface Asperities on Stick–Slip Behavior of Zinc-Coated Steel
Hao Gao, Qiang Wang, *et al.*
APRIL 05, 2023
LANGMUIR
READ

Enhanced Water Evaporation from Å-Scale Graphene Nanopores
Wan-Chi Lee, Kumar Varoon Agrawal, *et al.*
AUGUST 24, 2022
ACS NANO
READ

Get More Suggestions >

https://doi.org/10.1021/acs.jpcc.2c07081
J. Phys. Chem. C 2023, 127, 3671−3681